J. Fluid Mech. (2002), *vol.* 453, *pp.* 315–344.
DOI: 10.1017/S002211200100684X Printed in the United Kingdom

Moderate-Reynolds-number flow in a wall-bounded porous medium

By REGHAN J. HILL AND DONALD L. KOCH

School of Chemical Engineering, Cornell University, Ithaca, NY 14853, USA

(Received 14 September 2000 and in revised form 16 August 2001)

The transition to unsteady flow and the dynamics of moderate-Reynolds-number flows in unbounded and wall-bounded periodic arrays of aligned cylinders are examined using lattice-Boltzmann simulations. The simulations are compared to experiments, which necessarily have bounding walls. With bounding walls, the transition to unsteady flow is accompanied by a loss of spatial periodicity, and the temporal fluctuations are chaotic at much smaller Reynolds numbers. The walls, therefore, affect the unsteady flows everywhere in the domain. Consistency between experiments and simulations is established by examining the wake lengths for steady flows and the fundamental frequencies at higher Reynolds numbers, both as a function of the Reynolds number. Simulations are used to examine the velocity fluctuations, flow topologies, and the fluctuating forces on the cylinders.

1. Introduction

The lattice-Boltzmann method has recently gained popularity in computing finite-Reynolds-number flows in complex geometries, such as fixed arrays of solid particles (Koch & Ladd 1997; Ladd 1994*a*; Maier *et al.* 1998) and channel flows in which a relatively small number of particles are suspended and free to move (Qi 1999; Aidun, Lu & Ding 1998). Lattice-Boltzmann simulations of finite-Reynolds-number suspensions with enough particles to observe continuum behaviour have yet to be performed, but they will become feasible with the increasing availability of powerful computational resources. The interpretation of such simulations will be facilitated by an understanding of how fluid inertia at moderate Reynolds numbers affects flows in much simpler geometries.

The transition to unsteady flow in porous media has important practical implications for dispersion and heat and mass transfer. Unsteady flows typically occur at Reynolds numbers where convective transfer dominates molecular diffusion, i.e. the Péclet number, $Pe = Rev/D_m$, is much greater than one. Here, $Re = Ua/v$ is the Reynolds number, where a is the particle radius, U is the average velocity, v is the fluid kinematic viscosity, and D_m is the tracer molecular diffusivity. In liquids, $D_m/v \ll 1$, and hence the Péclet number may be large even when the Reynolds number is small. However, in gases, $D_m/v = O(1)$ and, hence, $Pe = O(Re)$, so transport at large Péclet numbers is accompanied by finite-Reynolds-number hydrodynamics.

Simulations of moderate-Reynolds-number flows in close-packed arrays of spheres show that unsteady flows can exist at Reynolds numbers as small as approximately 30 (Hill, Koch & Ladd 2001*b*). Temporal velocity fluctuations will modify the thickness of thermal and concentration boundary layers at solid surfaces, as well as mix fluid that would otherwise be bounded by closed streamlines. These will change the rates

of heat and mass transfer, and tend to favour mechanical dispersion over hold-up dispersion (Koch & Brady 1985).

Most computational studies of finite-Reynolds-number flows in porous media have focused on the steady or time-averaged drag force on ordered and random arrays of cylinders and spheres (Hill *et al.* 2001*a*, *b*; Maier *et al.* 1998). Koch & Ladd (1997), Ghaddar (1995) and Bittleston (1986) have examined the transition to unsteady flow in two-dimensional arrays of aligned cylinders using lattice-Boltzmann, finite-element and finite-difference methods, respectively. Bittleston also performed experiments to visualize steady wakes and to investigate flows that were forced with an oscillating pressure gradient. However, no quantitative comparisons of computations and experiments have been made, particularly concerning details of the transition to unsteady flow and the effects of bounding walls. This is due, in part, to the difficulty of obtaining such detailed information from experiments, as well as the high computational cost of accurately computing finite-Reynolds-number flows and dispersed two-phase flows at continuum length scales.

Since the dynamics of unsteady moderate-Reynolds-number flows depend on the underlying spatial velocity fluctuations, one means of testing the lattice-Boltzmann method at moderate Reynolds numbers, without having to directly compare the computed velocity fields with experiments, is to compare with experiments the critical Reynolds number for the transition to unsteady flow and the fundamental frequencies of the ensuing dynamics. These quantities are considerably easier to obtain from experiments, and, together, they allow both the temporal and spatial accuracy of the computations to be tested quantitatively.

The goal of this work, therefore, is to observe and quantify the dynamics of moderate-Reynolds-number flows using the lattice-Boltzmann method, and in doing so to examine how the simulations compare with experiments. The two-dimensional geometry used in this study provides a relatively simple and convenient means of comparing simulations with experiments. To avoid the complications of symmetry breaking, the pressure gradient is directed so the angle between the spatially averaged velocity and the primary axis of a square array of aligned cylinders is $\pi/6$. Comparing simulations and experiments requires simulations to be performed in which an otherwise unbounded periodic array of aligned cylinders is bounded by the walls of a straight channel.

An important consequence of spatial periodicity is that, when the flow through such an array is unsteady, there are fluctuating components of the average velocity in all directions. These are incompatible with the presence of bounding walls, and hence significant differences between simulations of unsteady moderate-Reynolds-number flows in unbounded periodic arrays of cylinders and wall-bounded flows are expected. For steady flows, the spatial accuracy of the simulations is tested by comparing with experiments the dependence of the length of the recirculating flow in the wakes of the cylinders upon the Reynolds number. At larger Reynolds numbers, the fundamental frequencies of the temporal fluctuations are compared, and consequently the bounding walls are found to have a significant effect on the spatial and temporal development of the flows.

The lattice-Boltzmann method and the computational methodology are described in §§ 2 and 3, respectively. The numerical accuracy of the simulations is dealt with in § 4, particularly the effects of fluid compressibility, which are found to be important in this work because of the cross-stream pressure gradient. The experimental and computational results are presented in the remaining §§ 5–10; these address the experiment, the topology of the steady flows, dynamics, the topology of the unsteady

flows, velocity fluctuations, and the drag forces on the cylinders, respectively. A summary follows in § 11.

2. The lattice-Boltzmann method

The lattice-Boltzmann method used in this work is discussed in detail by Ladd (1994*a,b*), and hence only a brief description is given here. Approximate solutions of the incompressible Navier–Stokes equations are sought from the moments of a discretized fluid-particle velocity distribution function. In three dimensions, there are 18 fluid-particle population densities at each node of a cubic lattice that extends throughout the computational domain. The population densities correspond to velocities in the directions to the six nearest and twelve next-nearest neighbouring lattice nodes. In this work, a three-dimensional formulation is used to compute two-dimensional flows by setting the length of the computational domain in the third spatial dimension (the z-direction) to one lattice unit, and applying periodic boundary conditions.

At each time step, the population densities are updated by performing collision and streaming steps, which relax the fluid-particle velocity distribution function toward equilibrium, and in doing so approximate solutions of the incompressible Navier–Stokes equations on macroscopic length and time scales. The pressure and velocity are obtained from the zeroth and first moments of the fluid-particle velocity distribution function and the ideal-gas equation of state relating the density to the pressure. Compressibility errors are of the order of the Mach number squared, which can be kept small while increasing the Reynolds number by either decreasing the fluid viscosity or increasing the ratio of the cylinder radius to the lattice-node spacing.

The kinematic viscosity and sound speed are made dimensionless with the lattice-node spacing and the time step. In this work, the dimensionless kinematic viscosity and sound speed are 0.01 and $1/\sqrt{2}$, respectively. This choice is based on considerations of numerical stability and computational efficiency (Ladd 1994*a*). In simulating flow past a sphere with a radius of 1 mm and a fluid kinematic viscosity of $10^{-6}\,\mathrm{m^2\,s^{-1}}$, for example, the lattice-Boltzmann time step corresponds to 10^{-4} s and the sound speed is $0.707\,\mathrm{m\,s^{-1}}$. While this sound speed is low, the Mach number is still sufficiently small (approximately 0.014) at a Reynolds number of 10, for example, for the fluid to be considered incompressible. Note also that 10^4 time steps are required for each characteristic viscous time a^2/ν. This example shows that the lattice-Boltzmann method tends to provide excellent time resolution, but does become limited at larger Reynolds numbers by spatial resolution and the fluid's compressibility. In practice, poor spatial resolution tends to coincide with, or is preceeded by, a loss of numerical stability, but compressibility artifacts are more difficult to identify (see § 4).

Boundary nodes, which represent the surface of the cylinders, are placed halfway along the links between the lattice nodes that intersect the cylinder surfaces. To ensure that the fluid velocity is zero at the cylinder surfaces, the fluid-particle population densities are propagated in the opposite direction to that from which they approach the boundary nodes. The hydrodynamic drag force on the cylinders is calculated by summing the impulses exerted on the cylinders by the fluid particles. As a result of the cubic lattice, the cylinders are not exactly cylindrical, and therefore an effective hydrodynamic radius must be determined by finding the small correction to the nominal cylinder radii of $j + 0.5$ lattice units ($j = 0, 1, 2 \ldots$) required for the Stokes-flow drag force on the cylinders in dilute square arrays to agree with the theories of Hasimoto (1959) and Sangani & Acrivos (1982). In this work, with the fluid kinematic viscosity equal to 0.01, and for cylinders with their centres at lattice nodes,

the effective hydrodynamic radii of cylinders with nominal radii larger than 2.5 lattice units are $j + 0.8$ lattice units ($j = 3, 4, 5 \ldots$) (Ladd 1994*b*; Koch & Ladd 1997).

3. Simulation methodology

The porous media considered in this work are square arrays of impermeable cylinders with a solid volume fraction

$$c = n\,\pi a^2 = \pi(a/L)^2, \tag{1}$$

where n is the cylinder number density, a is the cylinder radius, and L is the cylinder separation. Most of the simulations of flows in an unbounded periodic array of cylinders were performed with a single unit cell. However, to test the stability of these flows to disturbances with longer wavelengths, computations with four unit cells were performed. The nominal solid volume fraction of all the arrays considered in this work is 0.2.

Simulations with 26 cylinders in the computational domain and with bounding walls at $y = \pm H/2$ were also performed. Here, H is the width of the channel with walls parallel to the x-axis. The coordinate systems and the positions of the cylinders in the domains are shown in figure 1. Note that the primary axis of the cylinder array is directed at an angle of $\pi/6$ from the walls, and hence the effective length of the repeating unit cell in the direction perpendicular to the channel walls is $L\sin(\pi/6) = L/2$, which is 1/10th of the channel width. This choice was based on a compromise between minimizing the number of cylinders used in the experiment and simulations, and minimizing the direct influence of the walls on the bulk flow. While the underlying geometry of the cylinder array is not continuous across the left- and right-hand sides of the domain, visualizations of the flows (see figure 19, for example) show that the slight irregularity has a small effect on the resulting fluid velocity disturbances.

For the unbounded periodic arrays of cylinders, the x- and y-directions correspond to the $(1,0)$ and $(0,1)$ directions of the arrays, respectively. For the wall-bounded arrays, however, the x- and y-directions correspond to the directions parallel and perpendicular to the walls, respectively (see figure 1). In both cases, the directions parallel and perpendicular to the average velocity will be referred to as the streamwise and cross-stream directions, denoted with the subscripts $\parallel$ and $\perp$, respectively.

The lattice-Boltzmann method, described in the previous section, is used to compute the fluid velocity and the drag forces on the cylinders. The fluid is typically accelerated from rest by a constant body force. This is equivalent to applying a constant pressure gradient to the fluid, and, furthermore, allows periodic boundary conditions to be applied.

The Reynolds number is defined as

$$Re = |\langle \boldsymbol{u} \rangle| a/\nu, \tag{2}$$

where ν is the fluid kinematic viscosity, and $\langle \boldsymbol{u} \rangle$ is the temporally and spatially averaged velocity, which is equivalent to the so-called *superficial* velocity measured in an experiment by dividing the volumetric flow rate by the cross-sectional area of the containing vessel. The average velocity in the space occupied by the fluid is simply $\langle \boldsymbol{u} \rangle/(1-c)$.

At finite Reynolds numbers, the average velocity is not necessarily in the same direction as the average pressure gradient. When considering flow in an unbounded array of cylinders, the applied body force is directed at an angle θ_p from the x-axis – the (1,0)

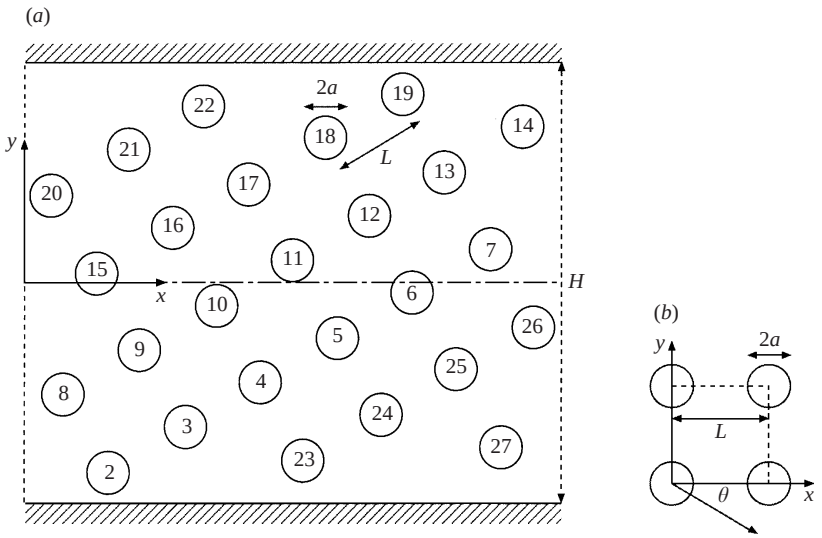

FIGURE 1. The computational domains used for the lattice-Boltzmann simulations of flows in (*a*) a wall-bounded array of cylinders and (*b*) an unbounded periodic array of cylinders. In both cases, the primary axis of the arrays is directed at an angle of $\pi/6$ from the flow direction. Periodic boundary conditions apply at the bounds of the domains (dashed lines), with the no-slip boundary condition at the top and bottom of the domain shown in (*a*).

direction of the square array – to achieve an angle θ_u between the spatially averaged velocity and the x-axis of $\pi/6$. Note that $\theta_u = \arctan(\langle u_y \rangle / \langle u_x \rangle)$ cannot be specified *a priori*, and hence trial-and-error was required to determine the appropriate θ_p to achieve a given θ_u. In general, the values of θ_u obtained were within approximately 3% of $\pi/6$. When more accurate results were required, linear or quadratic interpolation was used to determine properties of the flows at $\theta_u = \pi/6$.

The dimensionless drag force on the cylinders is defined as

$$F = |\langle \boldsymbol{f} \rangle| / (\mu |\langle \boldsymbol{u} \rangle|), \tag{3}$$

where $\langle \boldsymbol{f} \rangle$ is the spatially and temporally averaged drag force (per unit length) on the cylinders, and μ is the fluid dynamic viscosity. At steady state, the average drag force multiplied by the cylinder number density is equal to the average pressure gradient. From (1) and (3), it follows that the magnitude of the average pressure gradient is

$$|\langle \nabla p \rangle| = cL\mu v F |\langle \boldsymbol{u} \rangle| / (\pi a^2). \tag{4}$$

When the flow is unsteady at long times, the fundamental frequency of the fluctuating spatially averaged velocity and drag forces on the cylinders may be characterized by a Strouhal number,

$$S = \omega_1 a^2 / (vRe) = \omega_1 a / |\langle \boldsymbol{u} \rangle|, \tag{5}$$

where ω_1 is the fundamental frequency. In this work, the fundamental frequency will more often be non-dimensionalized with the inverse of the viscous time scale a^2/v. This choice reduces the uncertainty in the reported experimental results, since the errors in a and v are fixed, at least for the experiments performed with the same water temperature and, hence, viscosity, whereas the uncertainty in $|\langle \boldsymbol{u} \rangle|$ has contributions from systematic and statistical errors in the measured discharge flow rate, or Reynolds number.

4. Analysis of fluid compressibility and numerical accuracy

Simulations with various cylinder radii were performed to determine the effect of changing the grid resolution on the frequencies and amplitudes of the spatially averaged velocity fluctuations. Simulations of flows in unbounded periodic arrays were also performed with four unit cells in the computational domain. These tests showed that the most significant effect of increasing the grid resolution is to allow larger Reynolds numbers to be achieved before the onset of numerical instability, rather than significantly affecting the accuracy of the results. Furthermore, the simulations of flows in unbounded periodic domains with four unit cells gave identical velocity fields to those obtained from the simulations with a single unit cell, even at the highest Reynolds numbers where the velocity fluctuations are chaotic. These comparisons are elaborated in the thesis of Hill (2001).

In the remaining part of this section, the origin of spurious fluctuations in the spatially averaged cross-stream momentum, which occur when the computational domain is bounded by channel walls, is elucidated. With bounding walls, the deviation of the primary axis of the cylinder array from the walls induces a mean pressure gradient across the channel. Since the pressure is proportional to the density, this pressure gradient is accompanied by a density gradient. For unsteady flows, the fluctuating density gradient gives rise to a fluctuating spatially averaged cross-stream momentum, which, for an incompressible fluid, should be identically zero.

Note that the cross-stream momentum, which we refer to as spurious here, would not be identically zero for a real compressible fluid. Thus, while the lattice-Boltzmann method does give the correct qualitative behaviour (the lattice-Boltzmann method used in this work does not model the energy equation correctly) it does not describe compressible flows exactly. Nevertheless, our goal is to understand incompressible flows, and we have identified the compressibility of the fluid to be the most severe limitation on the numerical accuracy of our simulations of wall-bounded flows. In the following analysis, we show that compressibility does not necessarily affect the local fluid velocity fluctuations. Furthermore, based on the Mach number and the ratio of the cylinder radius to the lattice-node spacing, an upper limit on the width of the channel is established.

We examine perturbations to a base state whose density and velocity are given by $\rho_0 + y\alpha/c_s^2$ and $(U, 0)$, respectively. Here, α is the time-averaged cross-stream pressure gradient and U is the average fluid velocity, $|\langle \boldsymbol{u} \rangle|$. The ideal-gas equation of state relates the pressure and density fluctuations via $p' = c_s^2 \rho'$, where p' and ρ' are perturbations to the equilibrium pressure and density, respectively.

Substituting perturbations of the form $\rho' = y\alpha'(t)/c_s^2$ and (u', v') into the continuity equation, with $\alpha'(t)$ the perturbation to α, assuming that $H(\alpha + \alpha')/c_s^2 \ll \rho_0$, and neglecting streamwise gradients, the cross-stream momentum (per unit volume) resulting from the redistribution of mass across the channel width is

$$\rho_0 v' \sim -\tfrac{1}{2} c_s^{-2} \alpha_t' [y^2 - (\tfrac{1}{2}H)^2], \tag{6}$$

which, when integrated over the channel width, gives the fluctuating spatially averaged cross-stream momentum,

$$V(t)\rho_0 \sim -\tfrac{1}{12}(H/c_s)^2 \alpha_t', \tag{7}$$

where the subscript t indicates the time derivative. Averaging the square of (7) gives the standard deviation of V in terms of the standard deviation of α_t',

$$\langle V^2 \rangle^{1/2} \sim \tfrac{1}{12} U (MH/a)^2 \langle \Pi^2 \rangle^{1/2}, \tag{8}$$

H	Re	$\langle V^2\rangle^{1/2}a/v$	$\langle \Pi^2\rangle^{1/2}$
82	38	0.037	0.014
	51	0.097	0.015
	62	0.25	0.026
164	39	0.11	0.0088
	48	0.24	0.011
	58	0.53	0.013
	70	0.99	0.014
246	38	0.12	0.0049
	48	0.51	0.010
	55	3.3	0.044
	68	8.8	0.061

TABLE 1. The effect of channel width and Reynolds number on the cross-stream velocity fluctuations and scaled cross-stream fluctuating pressure gradient, from lattice-Boltzmann simulations of flow in a wall-bounded periodic array of cylinders with $a = 12.8$ lattice units.

where $M = U/c_s$ is the Mach number and

$$\Pi = \alpha'_t a^2/(\rho_0 U^3) \tag{9}$$

is a dimensionless α'_t, with the pressure gradient and time scaled with $\rho_0 U^2/a$ and a/U, respectively. It follows that $\langle \Pi^2\rangle^{1/2}$ should increase from zero at the critical Reynolds number to an $O(1)$ quantity at large Reynolds numbers.

To validate the scaling predicted by (8), a small number of simulations were performed with three channel widths of 82, 164 and 246 lattice units, all with cylinder radii of 12.8 lattice units. The cylinder configurations for these simulations were obtained by first discarding the cylinders in the upper third and two-thirds of the full domain shown in figure 1, and then displacing all the cylinders (by the same amount) perpendicular to the channel walls, so that the distance between the cylinders closest to the upper and lower walls were equal. Because we could not afford to increase the channel width beyond 246 lattice units, the resulting velocity fields cannot be expected to be self-similar with increasing channel width, and hence we should not expect the data from these simulations to collapse perfectly. However, the differences in the predicted $\langle \Pi^2\rangle^{1/2}$ should be much smaller than the corresponding variations in $\langle V^2\rangle^{1/2}$.

Table 1 shows $\langle \Pi^2\rangle^{1/2}$ given by (8), where $\langle V^2\rangle^{1/2}$ was obtained directly from the simulations for the three channel widths and various Reynolds numbers. Despite the systematic changes in $\langle V^2\rangle^{1/2}$ with H and Re, the corresponding variations in $\langle \Pi^2\rangle^{1/2}$ are relatively small – the exceptions will be discussed shortly. The partial collapse of the data confirms the scaling predicted by the theory, indicating that it captures the origin of the compressibility artifact as well as confirming that the velocity fields are incompressible on the length scale of the cylinder separation.

Note that an inertial scaling for the pressure gradient, $\alpha + \alpha' = O(\rho_0 U^2/a)$, allows the condition $H(\alpha + \alpha')/c_s^2 \ll \rho_0$ to be restated in terms of a constraint limiting the channel width for a given grid resolution (cylinder radius) and Reynolds (Mach) number, i.e. $H \ll a/M^2$. At a Reynolds number of 80, for example, the Mach number for a cylinder radius of 12.8 lattice units requires $H \ll 2000$ lattice units. The channel width used for these computations satisfies this constraint, and hence the density variations across the channel should be smaller than the nominal fluid

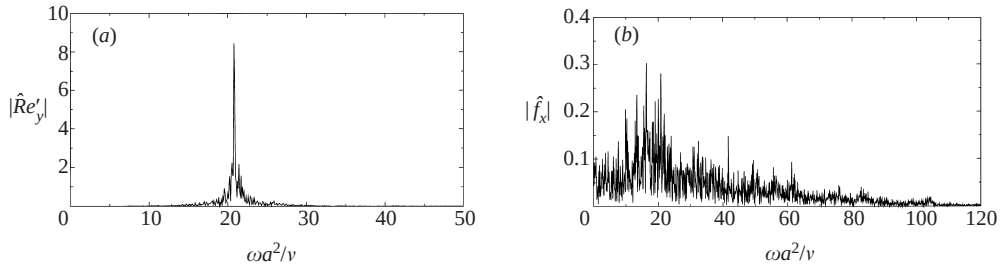

FIGURE 2. Fourier spectra of (*a*) the cross-stream component of the fluctuating average velocity, non-dimensionalized with ν/a to give a Reynolds number, and (*b*) the streamwise component of the fluctuating drag force (per unit length) on cylinder number 11 shown in figure 1. These results are from a lattice-Boltzmann simulation of flow in a wall-bounded periodic array of cylinders with $(c, a, H, Re) = (0.214, 12.8, 246, 68.4)$, where a and H are in lattice units. The energy of the fluctuating spatially averaged cross-stream momentum is contained in a small range of frequencies, and the small-scale velocity fluctuations, which affect the fluctuating forces on individual cylinders, are practically independent of the large-scale density fluctuations.

density. Clearly, increasing the Reynolds number requires either a narrower channel or a finer grid (larger a) to keep the density fluctuations small relative to the mean.

Note the ostensibly large values of $\langle \Pi^2 \rangle^{1/2}$ at the two largest Reynolds numbers for the simulations whose channel width is 246 lattice units. In these cases, we suspect that the fluctuating cross-stream momentum is amplified by a resonance of the underlying small-scale velocity fluctuations with the propagation of sound waves across the channel width. This explanation is based on the fact that the frequency corresponding to the time for disturbances travelling at the sound speed to traverse the channel width twice is $c_s/(2L) = 23.5\nu/a^2$, and, as shown in § 7.2.2, the fundamental frequency of the underlying velocity fluctuations reaches this resonant frequency when $Re \sim 70$.

Despite this resonance, the cross-stream momentum fluctuations in the widest channel, at Reynolds numbers greater than approximately 60, do not appear to significantly affect the small-scale velocity fluctuations. This is demonstrated by the comparison in figure 2 of the Fourier spectrum of the fluctuating spatially averaged cross-stream velocity with that of the fluctuating streamwise component of the force on a single cylinder, the latter providing a measure of the local velocity fluctuations. The energy in the fluctuating cross-stream momentum is contained in a small range of frequencies close to the resonant frequency, whereas the energy associated with the local velocity fluctuations is distributed over a much wider range of frequencies. This separation in time scales suggests that the local dynamics are not dominated by the large-scale density fluctuations.

There are, of course, components of the small-scale velocity fluctuations that are coupled to the spurious cross-stream momentum flux, particularly in the cross-stream direction (see figure 13). However, the energy contained in these modes, at the large Reynolds numbers where the resonance occurs, is small compared to the total fluctuating energy. In conclusion, these results show that care must taken when interpreting the Fourier spectra not to mistake the typically large peak, whose frequency is practically independent of the Reynolds number, for the fundamental frequency of the underlying small-scale velocity fluctuations. In general, this is difficult, because this peak is amplified when the fundamental frequency is close to that for sound waves to traverse the channel width twice.

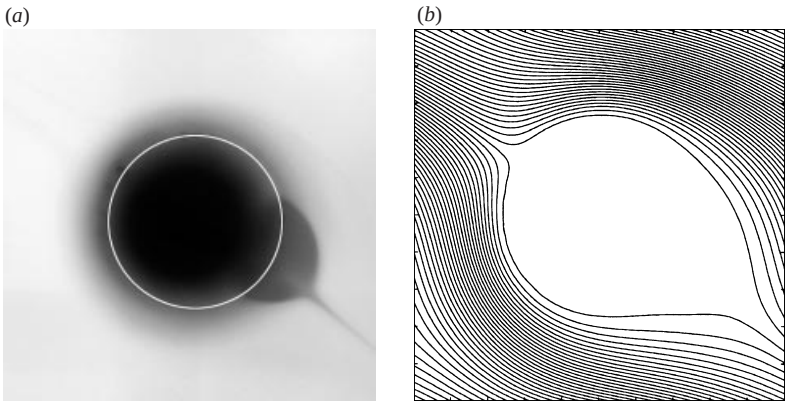

FIGURE 3. (*a*) A typical photographic image of the recirculating flow behind a cylinder close to the centreline of the channel used in the experimental apparatus $(a, c, Re, l/(2a)) = (2.5\,\mathrm{mm}, 0.196, 10 \pm 1, 0.25 \pm 0.02)$. (*b*) Streamlines obtained from a lattice-Boltzmann simulation of flow in an unbounded periodic array of cylinders with a similar Reynolds number to the flow visualized in (*a*).

5. Experiment

The experimental apparatus consisted of a long square channel whose internal dimensions were $5\,\mathrm{cm} \times 5\,\mathrm{cm} \times 100\,\mathrm{cm}$. Inside, approximately 510 brass cylinders, with an outside diameter of 5 mm, were fixed in a square array by inserting their ends into holes drilled into two opposite walls of the channel. The primary axis of the array was directed at an angle of $\pi/6$ from the channel walls. To highlight the regions of recirculating flow in the wakes of the cylinders, food colouring, diluted with water, could be continuously injected into the flow from the tip of an hyperdermic needle.

At Reynolds numbers close to the critical Reynolds number, the dominant frequency of the fluid velocity fluctuations could be determined by measuring the time for a fixed number of oscillations in the wakes. Typically, 10–30 oscillations were counted, using either a stop-watch or a high-speed camera.

The length of the steady wakes behind the cylinders was determined by taking still photographs of the dye tracer in the flow and scaling the wake length, as seen in the digital images, with the corresponding cylinder diameter. The length of the wakes is defined as the distance from the cylinder surface, along a straight line bisecting the cylinder, to the downstream tip of the wake.

At the smallest Reynolds numbers, the wakes behind the cylinders close to the channel centreline were most easily visualized by injecting a pulse of dye into the flow. Since dye in the steady wakes is bounded by closed streamlines, these wakes appeared dark against a light outer flow in which the dye was rapidly convected downstream. Figure 3 shows a typical example of a photographic image (*a*) of the wake behind a cylinder close to the channel centreline. This is compared with the streamlines obtained from a simulation (*b*) with a similar Reynolds number. Molecular diffusion allows a small quantity of dye to diffuse from the downstream tip of the wake, making the tip appear slightly longer and more pointed than it actually is.

At larger Reynolds numbers, it was convenient to release a continuous stream of dye into the flow. In this case, molecular diffusion, together with the slowly moving fluid close to the cylinder surfaces, allowed the dye to disperse around the upstream surfaces of the cylinders. Consequently, the wakes appeared light with a relatively dark outline. Again, a small quantity of dye diffused across the streamlines that separate the recirculating wake region from the outer flow.

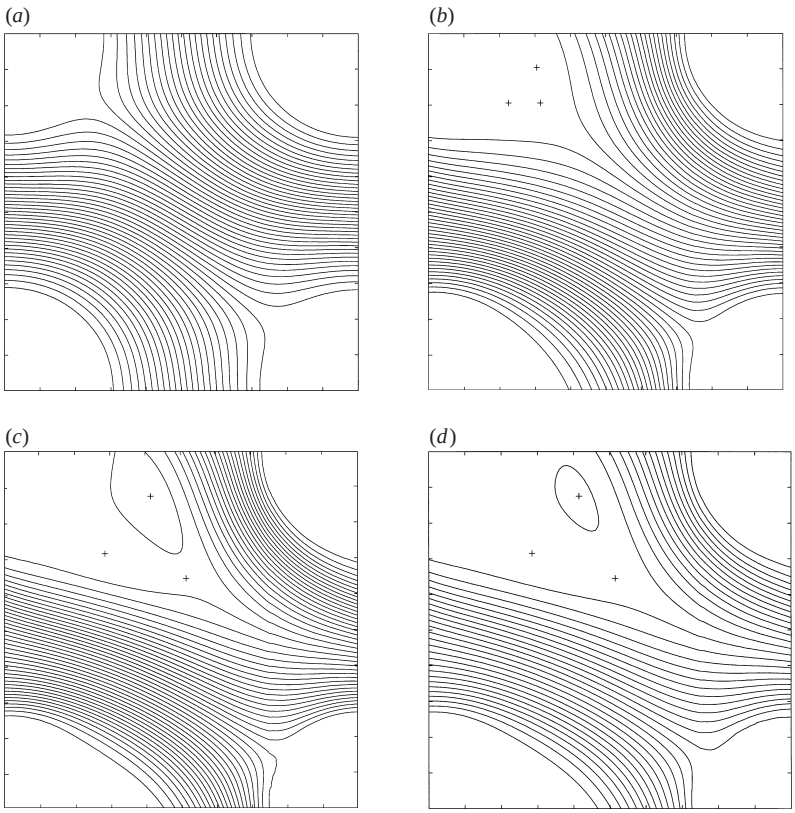

FIGURE 4. Streamlines from lattice-Boltzmann simulations of Stokes flow and steady finite-Reynolds-number flows in an unbounded periodic array of cylinders with $(c, \theta_u, a) = (0.193, \pi/6, 24.8)$, where a is in lattice units. The crosses identify the downstream tips of the wakes and the centres of the two counter-recirculating vortices. (*a*) $Re = 0$, (*b*) $Re = 11.7$, (*c*) $Re = 21.0$, (*d*) $Re = 32.0$.

The largest source of uncertainty in determining the wake lengths from the photographic images came from identifying the cylinder surfaces, which, as shown in figure 3, were blurred because of the finite depth-of-field. While some errors have fixed absolute values, and others have fixed relative values, no attempt was made to separate the systematic and statistical errors in the measured quantities.

The experimentally determined wake lengths, for steady flows, and the frequency of the oscillations in the unsteady wakes, are compared to those from lattice-Boltzmann simulations in figures 5 and 9, respectively. Here, we note that the transition to unsteady flow occurred at a critical Reynolds number of approximately 33 ± 3, and that the dimensionless fundamental frequency at the onset of unsteady flow was approximately 9 ± 1 (Hill 2001).

6. Wake length and topology for steady flows

Wake lengths from the simulations were determined by locating positions where both the x- and y-components of the velocity changed sign. For steady flows, such points identify the location of the downstream tips of the wakes and the centres of the two counter-recirculating vortices.

Figure 4 shows streamlines from simulations of steady flows in unbounded periodic

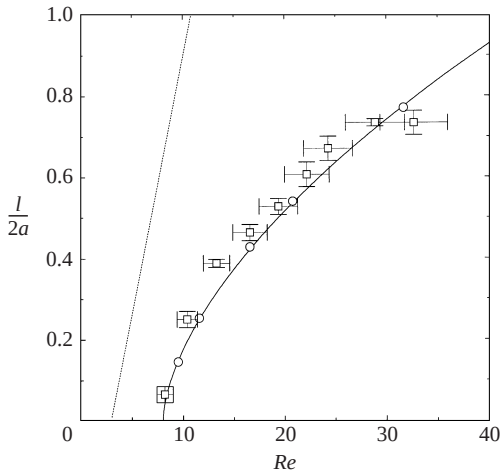

FIGURE 5. The dimensionless length of the recirculating flow attached to the rear of the cylinders as a function of the Reynolds number. The squares are from experiments, and the circles are from lattice-Boltzmann simulations of flows in an unbounded periodic array of cylinders with $(c, \theta_p, a) = (0.193, \pi/6, 24.8)$, where a is in lattice units. The solid line is the power-law fit given by (10), and the dotted line is a linear fit (11) to the experimental results of Taneda (1956) for a single cylinder in an unbounded fluid.

arrays of cylinders. The downstream tips of the wakes and the centres of the two counter-recirculating vortices are identified with crosses. In this geometry, the length of the wakes is limited by the competition between the slowly recirculating flow and the rapidly moving outer flow to fill the gaps between the cylinders. The wakes shown in figure 4 are considerably more elongated at larger Reynolds numbers than those for flow along the primary axis of symmetry of a body-centred array of cylinders (Bittleston 1986).

The length of the steady wakes is shown as a function of the Reynolds number in figure 5. The simulation results (circles) are given to a good approximation by the power-law fit

$$l/(2a) = 0.401(Re/8.07 - 1)^{0.6}, \tag{10}$$

suggesting that streamlines first separate from the cylinders at a Reynolds number of approximately 8.1. The good agreement between the simulations and experiments (squares) confirms the accuracy of the simulations, and shows that the effect of the bounding walls can be neglected near the channel centreline. The critical Reynolds number beyond which the flow is unsteady is approximately 34.6, and hence the dimensionless wake length at the transition to unsteady flow is $l/(2a) = 0.82$.

Taneda (1956) measured the wake length for a single cylinder in a practically unbounded fluid. From his experimental results, the wake length is given to a good approximation by the fit

$$l/(2a) = 0.377(Re/3.0 - 1), \tag{11}$$

which is shown as the dotted line in figure 5. For a single cylinder, the critical Reynolds number for the transition to unsteady flow is approximately 25 (Williamson 1989), and hence the dimensionless wake length at the transition to unsteady flow is $l/(2a) = 2.76$.

Bittleston (1986), using finite-difference computations, found a nonlinear dependence

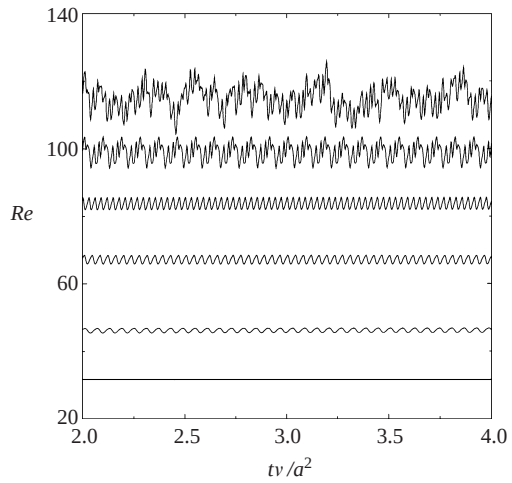

FIGURE 6. Time series of the spatially averaged velocity, non-dimensionalized with v/a to give a Reynolds number, from lattice-Boltzmann simulations of flows in an unbounded periodic array of cylinders with $(c, \theta_u, a) = (0.193, \pi/6, 24.8)$, where a is in lattice units. For the simulation with a time series chaotic, the Reynolds number is approximately 115 and $(c, \theta_u, a) = (0.194, \pi/6, 41.8)$.

of the wake length on the Reynolds number for flow along the primary axis of symmetry of a body-centred array of aligned cylinders with a solid volume fraction of 0.0765, with a cylinder separation in the flow direction 2.53 times that in the cross-steam direction. A critical Reynolds number was not identified, but the flow remained steady at Reynolds numbers up to 80, and the dimensionless wake length approached a constant close to one.

Clearly, the geometry of the array, and the direction of the flow relative to it, play an important role in determining the shapes of the wakes attached to the cylinders. Confining the wakes decreases their length and increases the Reynolds number at which streamlines first separate from the cylinders. Furthermore, increasing the slenderness of the steady wakes, as measured by the ratio $l/(2a)$, tends to decrease the critical Reynolds number. Therefore, the transition to unsteady flow in square arrays of cylinders, for example, might be expected to occur at larger Reynolds numbers when the flow is directed along the primary axis. Increasing the solid volume fraction should have a similar effect, provided that the structure of the wakes does not change significantly on increasing the solid volume fraction.

7. Dynamics

For unbounded periodic arrays of cylinders, the average velocity undergoes approximately sinusoidal oscillations at relatively low Reynolds numbers, with an amplitude that increases with the Reynolds number. As can be seen in figure 6, the dominant frequency also increases with the Reynolds number, and modes with both higher and lower frequencies are excited at larger Reynolds numbers (see figure 7). Period-doubling occurs at Reynolds numbers between approximately 85 and 115. Unfortunately, it is computationally impractical to determine the Reynolds numbers at which the bifurcations occur, because small changes in the direction of the applied pressure gradient, or body force, result in large changes in the flow direction, particularly at the higher Reynolds numbers.

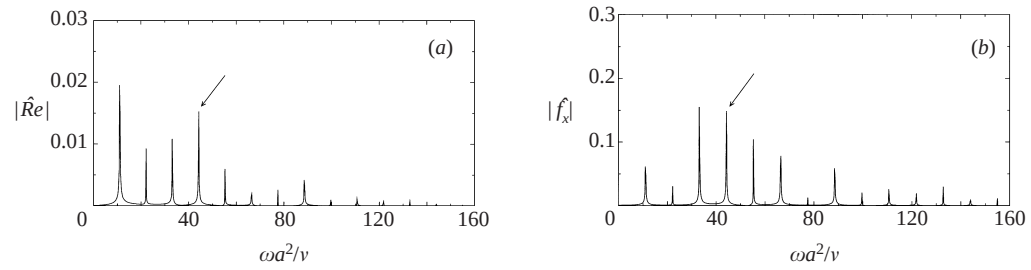

FIGURE 7. Fourier spectra of (*a*) the fluctuating spatially averaged velocity and (*b*) the *x*-component of the fluctuating drag force from a lattice-Boltzmann simulation of flow in an unbounded periodic array of cylinders with $(Re, c, \theta_p, \theta_u, a) = (100, 0.193, 0.80\,\pi/4, 0.689\,\pi/4, 24.8)$, where a is in lattice units. The arrows identify peaks corresponding to the fundamental frequency, whose dependence on the Reynolds number is shown in figure 9. The time series from which these spectra were obtained were first divided by their respective time-averaged values and then the mean was subtracted.

Fourier spectra of the spatially averaged velocity and the drag force on a single cylinder in an unbounded periodic array of cylinders are shown in figure 7. While the relative strength of the various Fourier modes in each spectrum may be different, the fundamental frequency can still be easily identified. Clearly, the transition from periodic to chaotic flow occurs via period-doubling as opposed to quasi-periodic dynamics, similarly to when the direction of the average pressure gradient is fixed (Koch & Ladd 1997).

7.1. *Hopf bifurcation*

The transition to unsteady flow occurs through the weakly nonlinear interaction of two spatial modes whose amplitudes fluctuate sinusoidally in time. The amplitude of the fluctuating spatially averaged velocity, non-dimensionalized to give a Reynolds number, is given to a good approximation by the fit

$$A_1 = 0.938(Re/34.6 - 1)^{1/2} + 0.396(Re/34.6 - 1), \tag{12}$$

which is shown in figure 8 as the solid line. The critical Reynolds number of 34.6 is in good agreement with the experimentally determined value of 33 ± 3.

Close to the critical Reynolds number, the amplitude of the fluctuating spatially averaged velocity increases with the square root of the Reynolds number. With reasonable certainty, therefore, the transition to unsteady flow in an unbounded periodic array of cylinders occurs via a *super-critical* Hopf bifurcation (Wiggins 1990). This excludes the possibility of observing unsteady flows at smaller Reynolds numbers. Such flows would require finite-amplitude disturbances to initiate them, and they would be considerably more difficult to examine, both computationally and experimentally.

The range of Reynolds numbers over which the scaling given by (12) is accurate corresponds to a small parameter $\epsilon = Re/Re_c - 1$ being less than approximately 0.05. The range of Reynolds numbers where the dynamics are dominated by the nonlinear interaction of only two unstable modes is therefore very small. At larger Reynolds numbers, the dynamics are dominated by the nonlinear interactions between an increasing number of unstable modes.

Schatz, Dwight & Swinney (1995) studied the transition to unsteady flow in a channel with a streamwise periodic array of cylinders close to one of the walls. Their experiments and computations show that unsteady flow develops at a Reynolds number based on the channel half-width of approximately 130. While they point

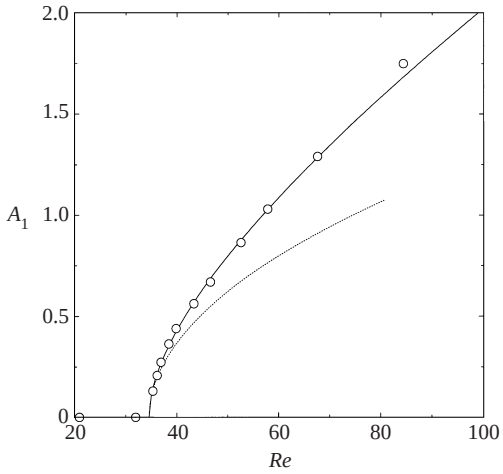

FIGURE 8. The amplitude of the fluctuating spatially averaged velocity, non-dimensionalized with v/a to give a Reynolds number, as a function of the Reynolds number based on the spatially and temporally averaged velocity. The symbols are from lattice-Boltzmann simulations of flows in an unbounded periodic array of cylinders with $(c, \theta_u, a) = (0.193, \pi/6, 24.8)$, where a is in lattice units. The solid line is the fit given by (12), and the dotted line is the first term in (12).

out that this Reynolds number is significantly smaller than that for the transition to turbulence in the absence of the cylinders, it is interesting to note that the Reynolds number based on the cylinder radius is about 26, which is close to the critical Reynolds number identified here – the weakly nonlinear regime also corresponds to a supercritical Hopf bifurcation. Thus, while the cylinder configuration in their study is very different to ours – the channel width was 10 times the cylinder radius – the global dynamics appear to be very much influenced by the velocity fluctuations at the length scale of the cylinders, rather than the channel width.

7.2. *Fundamental frequency*

Figure 9 compares the dimensionless fundamental frequency of unbounded and wall-bounded arrays of cylinders as a function of the Reynolds number. Despite the solid volume fractions being very close, the fundamental frequencies from the simulations of flows in unbounded arrays (circles) are significantly higher than those from the experiments (triangles), which, of course, have bounding walls. At the Reynolds numbers where the frequency increases linearly with the Reynolds number, the simulation results for wall-bounded flows, identified in figure 9 by the squares and diamonds for solid volume fractions of 0.214 and 0.249 are given to a good approximation by the fits $\omega_1 a^2/\nu = 0.303Re - 1.33$ and $\omega_1 a^2/\nu = 0.403Re - 1.93$, respectively. Assuming a linear dependence of the coefficients on the solid volume fraction, the dimensionless frequency at a solid volume fraction corresponding to that of the experiments ($c = 0.196$) is approximately $\omega_1 a^2/\nu = 0.252Re - 1.02$. This is in reasonable agreement with the experiments, which, in the range of Reynolds numbers 35–65, give $\omega_1 a^2/\nu = 0.290Re - 0.80$. Clearly, the fundamental frequencies of the flows with bounding walls are lower than predicted by the simulations of flows in unbounded periodic arrays.

With the onset of unsteady flow, the spatial periodicity of the wall-bounded flows is broken at the length scale of the cylinder separation. The resulting increase in the effective wake length is a likely explanation for the slower dynamics. Note that the

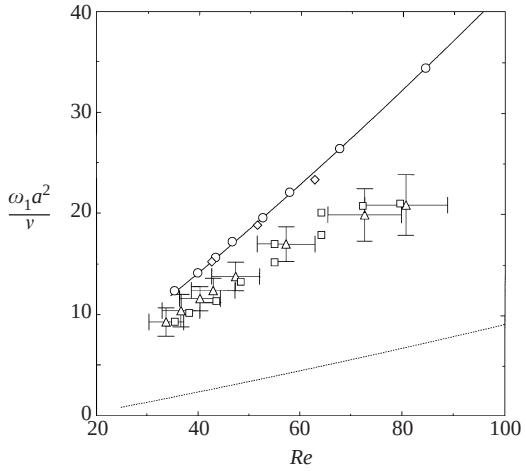

FIGURE 9. The dimensionless frequency of the fluctuating spatially averaged velocity as a function of the Reynolds number. The circles are from lattice-Boltzmann simulations of flows in an unbounded periodic array of cylinders with $(c, \theta_u, a) = (0.193, \pi/6, 24.8)$, where a is in lattice units, and the solid line is the fit given by (13). The triangles are from experiments ($c = 0.196$) and the squares and diamonds are from lattice-Boltzmann simulations of flows in a wall-bounded periodic array of cylinders with $(c, \theta_u, a) = (0.214, \pi/6, 12.8)$ and $(0.249, \pi/6, 13.8)$, respectively. The dotted line is from the experiments of Williamson (1989) for a single cylinder in an unbounded fluid given by (14).

Strouhal number, as defined by (5), compares the inverse fundamental frequency with the time for disturbances to convect a distance of one cylinder radius. If, however, the fundamental frequency is determined by the time it takes for disturbances to convect along the wakes, then the Strouhal numbers based on the wake length should be similar for flows with different wake lengths. At the transition to unsteady flow, for a single cylinder in an unbounded fluid and for the cylinder arrays examined here, the Strouhal numbers based on the wake lengths are 0.83 and 0.57, respectively. While these are not the same, they are much closer than those based on the cylinder radius. Consequently, the wake length provides a better estimate for the characteristic length scale of the instability than the cylinder radius (or channel width).

Before examining details of dynamics in the unbounded and wall-bounded domains separately, note that at Reynolds numbers greater than approximately 60, the fundamental frequency of the wall-bounded flows cannot be identified unambiguously. This is because the fluctuations are chaotic and their energy is distributed over a wide range of frequencies. It is not surprising, therefore, that it was also difficult to identify the fundamental frequencies experimentally, as suggested by the relatively large error bars at the largest Reynolds numbers in figure 9. The levelling-off of the experimentally determined fundamental frequency possibly reflects the higher weighting given to the lower-frequency, larger-amplitude modes. The almost constant frequency at the largest Reynolds numbers suggested by the simulations (squares), reflects the peak in the spectra from the spurious cross-stream momentum discussed in § 4. Recall that this frequency corresponds to the time for sound waves to traverse the channel width twice, and hence it is independent of the Reynolds number.

7.2.1. *Unbounded spatially periodic flows*

For flow in an unbounded periodic array of cylinders, increasing the Reynolds number increases the number of modes with both higher and lower frequencies

than the fundamental frequency. These can be identified most easily in the Fourier spectrum of the spatially averaged velocity shown in figure 7 and, possibly, in the time series of the spatially averaged velocities shown in figure 6. Until the onset of chaotic dynamics, which occurs at a Reynolds number in the range 85–115, all the frequencies in the spectra are commensurate with the fundamental frequency, confirming that the chaotic dynamics occur via a sequence of period-doubling bifurcations.

At Reynolds numbers greater than approximately 100, the flow in unbounded periodic arrays of cylinders is chaotic and the Fourier spectra have a continuous range of frequencies with distinct peaks. Indeed, some care was required to identify the peaks in the spectra corresponding to the fundamental frequency. In general, the fundamental frequency can be identified in the spectra of both the spatially averaged velocity and the drag force on the cylinders.

For unbounded periodic arrays of cylinders, the fundamental frequency increases linearly with the Reynolds number, with a small quadratic correction at larger Reynolds numbers. The simulation results identified with circles in figure 9 are given to a good approximation by the fit

$$\omega_1 a^2/\nu = 12.1 + 14.2(Re/34.6 - 1) + 0.924(Re/34.6 - 1)^2, \tag{13}$$

which is shown as the solid line. The critical Reynolds number in (13) was obtained from the dependence of the amplitude of the fluctuations on the Reynolds number, given by (12), and hence the Strouhal number at the critical Reynolds number is $\omega_c a^2/(\nu Re_c) = 12.1/34.6 = 0.35$.

The dotted line in figure 9 is the fit

$$\omega_1 a^2/\nu = -0.8316 + 0.0908Re + 1.6 \times 10^{-4} Re^2, \tag{14}$$

to the experimental results of Williamson (1989) for the fundamental frequency of the oscillations in the wake of a single cylinder in a practically unbounded fluid. The Strouhal number at the critical Reynolds number of 25 is 0.062. Clearly, in addition to increasing the critical Reynolds number, the confinement of the wakes in the cylinder arrays significantly increases the frequency of the oscillations. As mentioned above, this is expected based on the shorter wake length imposed by the confining geometry.

7.2.2. *Wall-bounded flows*

For wall-bounded flows at Reynolds numbers less than approximately 40, the dynamics eventually become periodic, whereas at larger Reynolds numbers, chaotic dynamics occur at much smaller Reynolds numbers than for unbounded periodic arrays (figure 6). Time series of the spatially averaged velocity, non-dimensionalized to give a Reynolds number, are shown in figure 10.

The Fourier spectrum of the time series at Reynolds number approximately 64.1 is shown in figure 11. The large peak at a dimensionless frequency of approximately 20 has already been associated with the time for sound waves to traverse the channel width twice. At this relatively large Reynolds number, where the dynamics are chaotic, the fundamental frequency is difficult to identify amongst the broad and continuous range of frequencies in the spectrum. Instead, it is helpful to examine the dynamics of the fluctuating forces on the cylinders, since these are more closely related to the local velocity fluctuations.

The fundamental frequencies in figure 9 were obtained from the time series of both the streamwise and cross-stream components of the drag force on cylinder number 11, whose position in the array is shown in figure 1. As the time series in figure 12 show, the fluctuating forces on the cylinders at relatively small Reynolds numbers

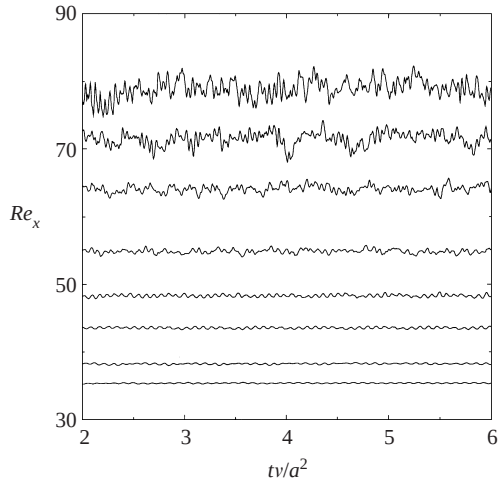

FIGURE 10. Time series of the spatially averaged velocity, non-dimensionalized with v/a to give a Reynolds number, from lattice-Boltzmann simulations of flows in a wall-bounded periodic array of cylinders with $(c, \theta_u, a) = (0.214, \pi/6, 12.8)$, where a is in lattice units. At Reynolds numbers less than approximately 40, the time series eventually become periodic. The Fourier spectrum of the time series from the simulation with a Reynolds number of approximately 64.1 is shown in figure 11.

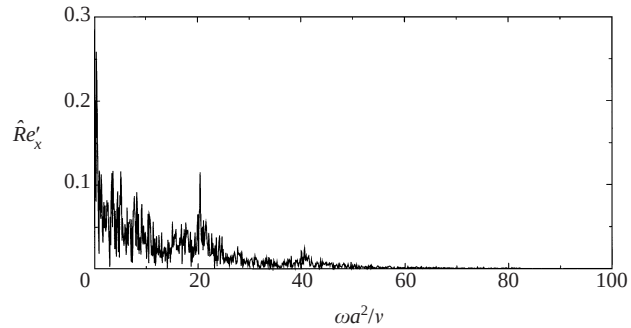

FIGURE 11. The Fourier spectrum of the streamwise component of the fluctuating spatially averaged velocity, non-dimensionalized with v/a to give a Reynolds number, from a simulation of unsteady flow in a wall-bounded periodic array of cylinders with $(Re, c, \theta_u, a) = (64.1, 0.214, \pi/6, 12.8)$, where a is in lattice units.

are almost periodic, but they are out of phase with one another. At larger Reynolds numbers, however, the fluctuations are chaotic and relatively independent, suggesting a breaking of the underlying spatial periodicity.

Figure 13 compares Fourier spectra of the time series of the streamwise and cross-stream components of the drag force on cylinder number 11 at Reynolds numbers of 43.5 and 64.1. At the smaller Reynolds number, the time series is not exactly periodic, but is dominated by a mode whose frequency is ω_1 and a higher-frequency harmonic whose frequency is $2\omega_1$. The satellite peaks in the spectra explain the amplitude-modulation of the time series shown in figure 12. At the larger Reynolds number, the frequency corresponding to the fluctuating spatially averaged cross-stream momentum is easily identified in the spectrum of the fluctuating cross-stream component of the drag force. In the streamwise direction, the peak with the largest amplitude corresponds to a dimensionless frequency of 17.9. The linear increase of the

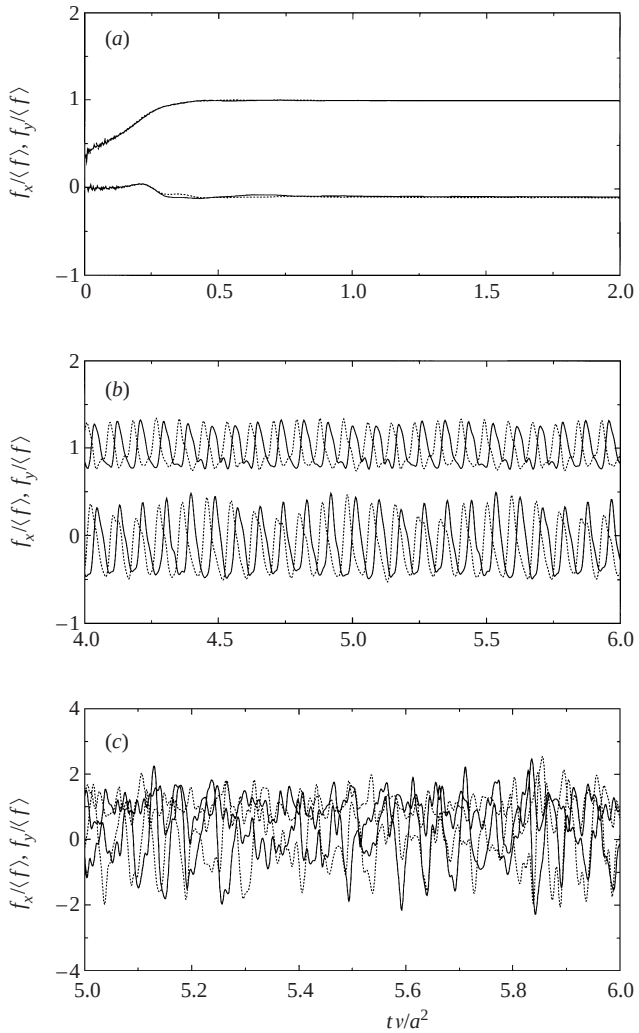

FIGURE 12. Time series of the streamwise (non-zero mean) and cross-stream (zero mean) components of the drag forces, non-dimensionalized with the average drag force, on two cylinders in the simulated channel flows. These results are from lattice-Boltzmann simulations of flows in a wall-bounded periodic array of cylinders with $(c, a) = (0.214, 12.8)$, where a is in lattice units. The solid and dotted lines identify cylinders 10 and 11, respectively, whose positions in the channel are shown in figure 1. (*a*) $Re = 25.4$ (steady), (*b*) $Re = 43.5$ ($\omega_1 a^2/v = 11.8$), (*c*) $Re = 79.5$.

fundamental frequency shown in figure 9, at the smaller Reynolds numbers, suggests that this is the fundamental frequency of the underlying velocity fluctuations at this Reynolds number.

8. Topology of unsteady flows

Figures 14–16 show streamlines of the flow in an unbounded periodic array of cylinders at nominal Reynolds numbers of 35, 45 and 85, respectively. Each snapshot of the flow corresponds to an equally spaced time throughout the fundamental period of the fluctuations. The streamlines were obtained from contours of the

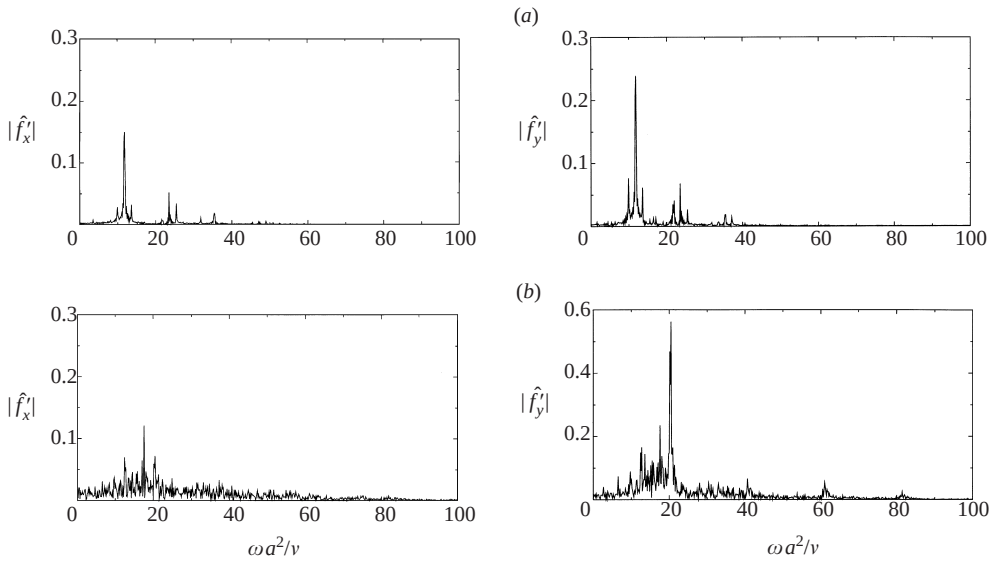

FIGURE 13. Fourier spectra of the streamwise (left) and cross-stream (right) components of the fluctuating drag force on cylinder number 11 obtained from lattice-Boltzmann simulations of flows in a wall-bounded periodic array of cylinders with $(c, a) = (0.214, 12.8)$. The spectra in (*a*) are representative of the behaviour at smaller Reynolds numbers (43.5) when the flow is quasi-periodic, whereas the spectra in (*b*) are representative of the behaviour at Reynolds numbers greater than approximately 50 (64.1) when the flow is chaotic. The time series from which these spectra were obtained were first divided by their respective time-averaged values and then the mean was subtracted.

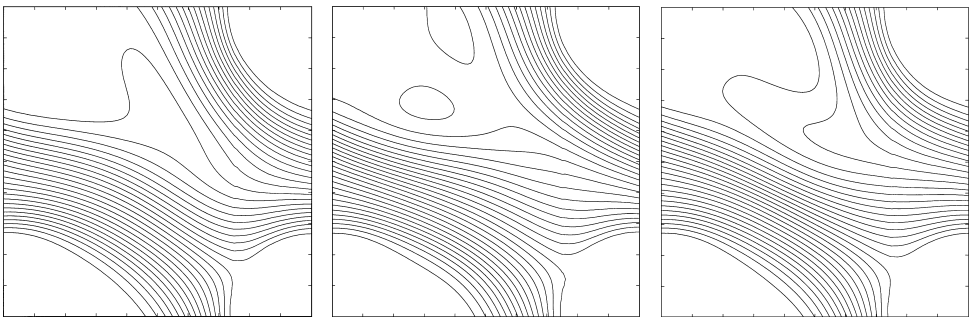

FIGURE 14. Streamlines obtained from lattice-Boltzmann simulations of unsteady flow in an unbounded periodic array of cylinders with $(Re, \theta_p, a, L) = (36.1, 0.81\,\pi/4, 24.8, 100)$, where a and L are in lattice units. In going from left to right, the time between each snapshot, Δt, is 2000 time steps, corresponding to $\Delta t\nu/a^2 = 3.26 \times 10^{-2}$.

stream function, ψ, which was calculated from the velocity field using the relations $\partial\psi/\partial y = u_x$ and $\partial\psi/\partial x = -u_y$.

At the smallest Reynolds number of 36.1, which is just above the critical Reynolds number of 34.6, the oscillating flow corresponds to a side-to-side waving of the wakes. As the sequence of images in figure 14 show, the displacement to each side is approximately the same. There is also evidence of a 'whipping' motion at the tip, where open streamlines are drawn backwards into a slowly moving region (widely separated streamlines) outside the wake. In between the extremities of the waving motion, the wake is similar in appearance to the steady wakes shown in figure 4.

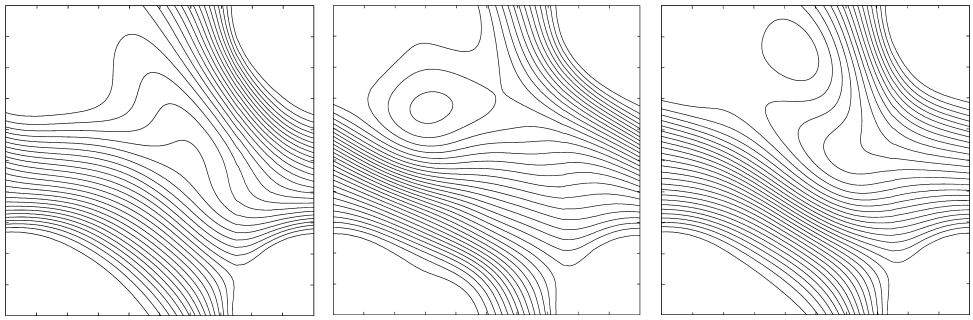

FIGURE 15. As figure 14 but with $(Re, \theta_p, a, L) = (46.6, 0.83\,\pi/4, 24.8, 100)$. In going from left to right, the time between each snapshot, Δt, is 1200 time steps, corresponding to $\Delta t v/a^2 = 1.95 \times 10^{-2}$.

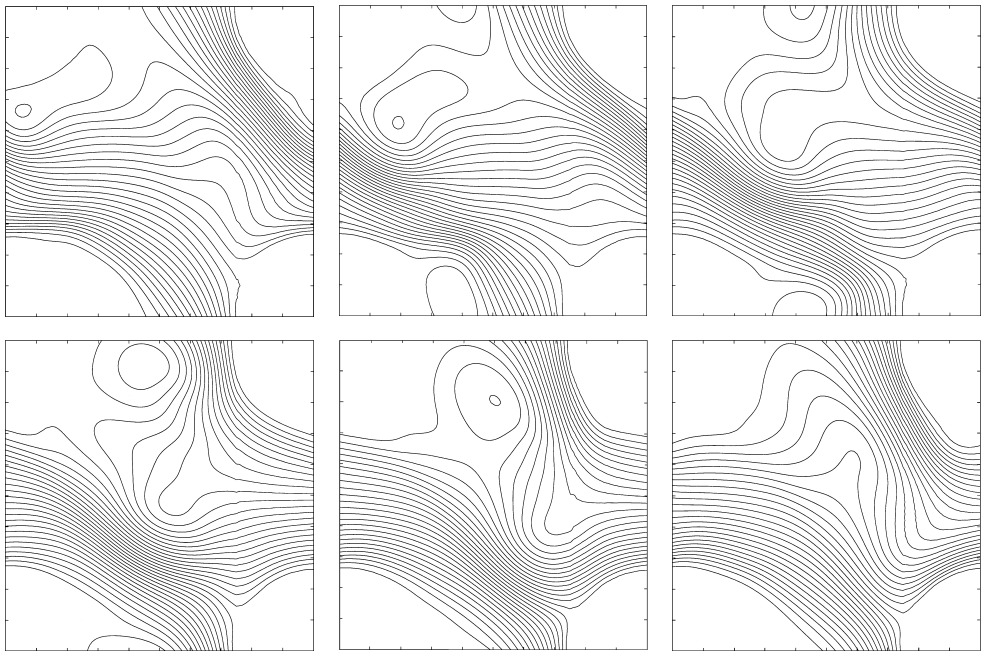

FIGURE 16. As figure 14 but with $(Re, \theta_p, a, L) = (84.4, 0.83\,\pi/4, 24.8, 100)$. In going from left to right and from top to bottom, the time between each snapshot, Δt, is 300 time steps, corresponding to $\Delta t v/a^2 = 4.88 \times 10^{-3}$.

At a larger Reynolds number of 46.6, vortices can be seen to shed from alternate sides of the cylinders. The images in figure 15 show the shedding of a vortex from the lower side of the cylinder. This sequence is similar to that of the remaining half of the cycle, in which a vortex is shed from the upper side (Hill 2001). In the image on the left, the vortex to be shed is still attached to the cylinder; it rapidly detaches, leading to the closed streamlines seen in the second image. In the third image, all that remains of the vortex is the region of distorted 'u'-shaped streamlines.

With increasing Reynolds number, the velocity disturbance where the streamlines separate furthest upstream from the cylinder surfaces increases. The streamlines separating the inner and outer regions of the wake show that the volume of fluid attached to the cylinders for any appreciable length of time is much smaller than when the wakes are stationary. As shown in figure 16, at a Reynolds number of

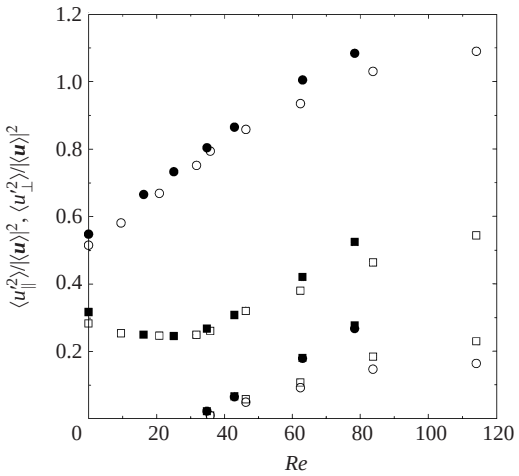

FIGURE 17. The variance of the streamwise (circles) and cross-stream (squares) components of the velocity in an unbounded periodic array of cylinders (open symbols) and a wall-bounded periodic array of cylinders (filled symbols). The upper two sets of symbols include both spatial and temporal fluctuations in the velocity, $\boldsymbol{u}-\langle\boldsymbol{u}\rangle = \boldsymbol{u}_1+\boldsymbol{u}_2$, whereas the lower two, which begin with zero amplitude at the critical Reynolds number of approximately 34, include only the time-dependent fluctuations of the velocity, $\boldsymbol{u}_2$. These results are from lattice-Boltzmann simulations with $(c, \theta_u, a) = (0.193, \pi/6, 24.8)$ (open symbols) and $(c, a) = (0.214, 12.8)$ (filled symbols), where a is in lattice units. For the simulation at Reynolds number approximately 115, $(c, \theta_u, a) = (0.194, \pi/6, 41.8)$.

84.4, this relatively small volume of fluid resides directly behind the cylinders, and is characterized by a thin pointed tail on one side and a detaching vortex on the other.

Recall that the time series of the spatially averaged velocity is chaotic at a Reynolds number of 116. Under these conditions, the sequence of alternate vortex shedding identified above, at Reynolds numbers up to approximately 85, cannot be identified unambiguously. Highly distorted vortices are seen to shed, with points of separation occurring further upstream (Hill 2001). Clearly, the length and time scales diminish with increasing Reynolds number, and hence the streamlines are increasingly distorted.

9. Spatial and temporal velocity fluctuations

The variances of the streamwise and cross-stream components of the velocity can be used to quantitatively compare the spatial and temporal velocity fluctuations of flows in wall-bounded and unbounded periodic arrays of cylinders. In this work, the velocity is decomposed as

$$\boldsymbol{u} = \langle\boldsymbol{u}\rangle + \boldsymbol{u}_1(\boldsymbol{x}) + \boldsymbol{u}_2(\boldsymbol{x}, t), \tag{15}$$

where $\langle\boldsymbol{u}\rangle$ is the spatially and temporally averaged velocity. Note that the spatial averages of $\boldsymbol{u}_1$ and $\boldsymbol{u}_2$, and the temporal average of $\boldsymbol{u}_2$, are zero.

Figure 17 shows the variance of the streamwise (circles) and cross-stream (squares) components of $\boldsymbol{u}_1 + \boldsymbol{u}_2$ and $\boldsymbol{u}_2$, as a function of the Reynolds number. The former is a measure of the combined spatial and temporal fluctuations in the velocity, whereas the latter quantifies only the temporal fluctuations. These results are from simulations of flows in a wall-bounded array of cylinders (filled symbols) and an unbounded periodic array of cylinders (open symbols). Spatial averaging was performed over the entire computational domain, and, depending on the Reynolds number, temporal

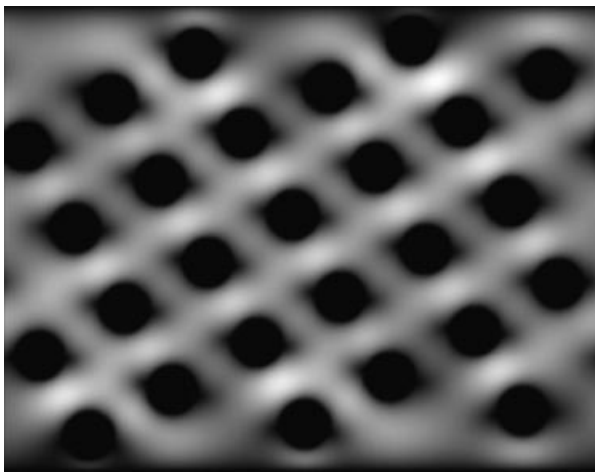

FIGURE 18. Grey-scale map of the magnitude of the velocity from a lattice-Boltzmann simulation of Stokes flow ($Re = 0$) in a wall-bounded periodic array of cylinders with $(c, a) = (0.214, 12.8)$, where a is in lattice units.

averages were obtained from between 10 and 100 snapshots of the flows at evenly spaced times spanning 1 to 4 periods of the fundamental oscillation. Including the volume of the domain occupied by the stationary cylinders in the averaging is merely for convenience. Values for the region occupied only by the fluid can be obtained by suitable algebraic manipulations of the defining volume integrals. Here, we are interested in examining relative rather then absolute values, and hence the distinction is not important.

The small difference between the variances for wall-bounded and unbounded spatially periodic flows when the Reynolds number is zero is because of the small difference in the solid volume fractions, as well as the discontinuity of the geometry at the bounds of the domain. With increasing Reynolds number, the distance over which the walls disturb the flow diminishes, and hence the contribution to the velocity variances from the inhomogeneity at the walls should diminish with increasing Reynolds number. The variances of the steady flows are practically the same, confirming that the walls do not affect the flow over most of the channel width. However, as the Reynolds number increases beyond the critical value, approximately 35, the variance of both the streamwise and cross-stream components of the velocity increase more rapidly when there are bounding walls. This is almost entirely because of the growth of the temporal fluctuations.

With bounding walls, the variance of the streamwise and cross-stream components of $\boldsymbol{u}_2$ are practically equal, whereas the cross-stream components are slightly larger in the absence of walls. This difference may be interpreted as the walls suppressing the temporal velocity fluctuations in the cross-stream direction more than in the streamwise direction. Note also that the fluctuating energy is partitioned equally in the streamwise and cross-stream directions, whereas the time-averaged spatial velocity fluctuations are considerably larger in the streamwise direction.

The velocity distribution for a Stokes flow ($Re = 0$) is shown in figure 18, where the light and dark tones correspond to high and low velocities, respectively. The velocity field is spatially periodic at the length scale corresponding to the cylinder separation, and has local for–aft symmetry about each of the cylinders. In contrast to

(*a*)

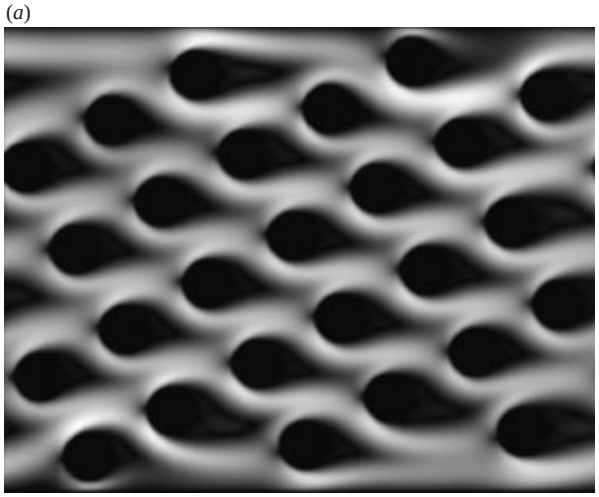

(*b*)

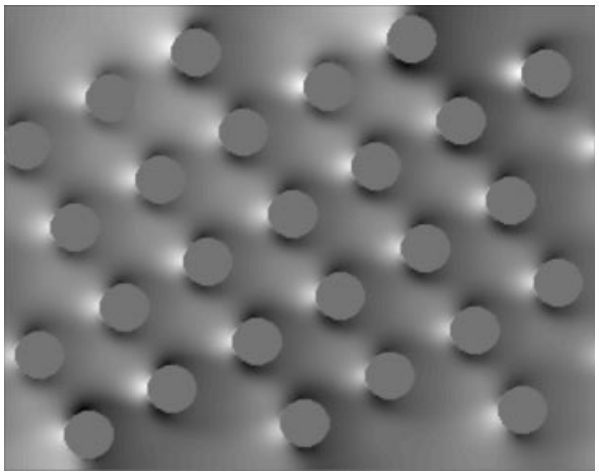

FIGURE 19. Grey-scale maps of (*a*) the magnitude of the velocity and (*b*) the spatial pressure or density fluctuations obtained from a lattice-Boltzmann simulation of a steady flow in a wall-bounded periodic array of cylinders with $(Re, c, a) = (25.4, 0.214, 12.8)$, where a is in lattice units.

the finite-Reynolds-number flows shown below in figures 19 and 20, the fluid velocity between the walls and the cylinders closest the walls is very slow.

At a Reynolds number of 25.4, the velocity distribution shown in figure 19(*a*) is also spatially periodic at the length scale corresponding to the cylinder separation, but obviously does not have local for–aft symmetry about each of the cylinders. The spatial distribution of the fluid density, which is proportional to the pressure, is shown in figure 19(*b*), where the light and dark tones correspond to high and low pressures, respectively. As expected from Bernoulli's equation for potential flow, the highest and lowest pressures occur on the upstream faces and sides of the cylinders, respectively.

At a Reynolds number of 79.5, where the temporal velocity fluctuations are chaotic, the spatial periodicity of the velocity field, as seen in the snapshot of the velocity distribution in figure 20(*a*), is broken. The time-averaged velocity field, whose velocity distribution is shown in figure 20(*b*), is spatially periodic at the length scale of the

(*a*)

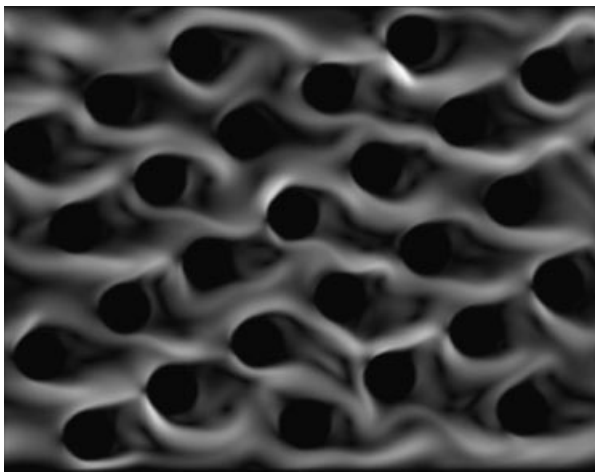

(*b*)

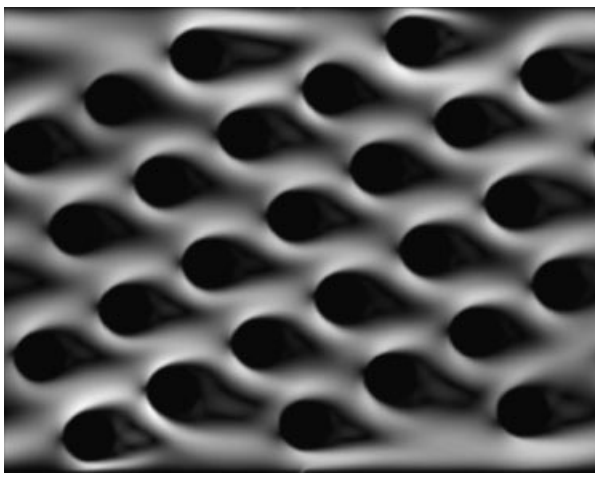

FIGURE 20. Grey-scale maps of the magnitude of the velocity from a lattice-Boltzmann simulation of unsteady flow in a wall-bounded periodic array of cylinders with $(Re, c, a) = (79.5, 0.214, 12.8)$, where a is in lattice units. The image in (*a*) is a snapshot of the flow, whereas the image in (*b*) is from the time-averaged velocity field.

cylinder separation. While the time-averaged velocity fields for unbounded periodic and wall-bounded flows are similar, the comparison of their velocity variances above (see figure 17) shows they are not the same.

10. Drag force

10.1. *Streamwise drag force*

The dimensionless drag force on the cylinders in wall-bounded and unbounded periodic arrays increases approximately linearly with the Reynolds number over a wide range of Reynolds numbers. The simulation results shown in figure 21 for cylinders in unbounded periodic arrays (circles) are given to a good approximation

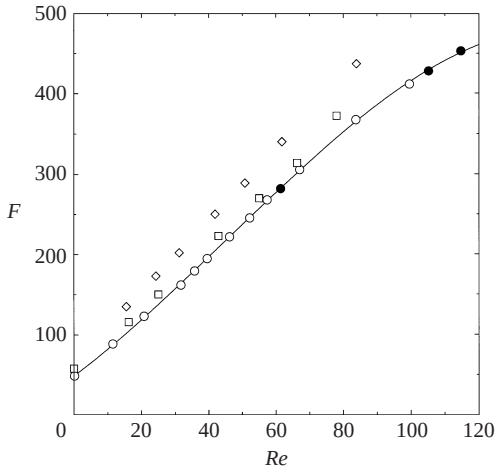

FIGURE 21. The dimensionless drag force as a function of the Reynolds number. The circles are from lattice-Boltzmann simulations of flows in unbounded periodic arrays of cylinders with $(a, \theta_u, c) = (24.8, \pi/6, 0.193)$ (open) and (41.8, $\pi/6$, 0.194) (filled), respectively, where a is in lattice units. The line is the fit given by (16), and the squares and diamonds are from simulations of flows in wall-bounded periodic arrays of cylinders with $(a, \theta_u, c) = (12.8, \pi/6, 0.214)$ and $(13.8, \pi/6, 0.249)$, respectively.

by the fit

$$F = 49.45 + 2.99Re + 0.0232Re^2 - 0.0001695Re^3. \tag{16}$$

Note that this equation does not have the correct asymptotic behaviour in the limit $Re \to 0$, which actually takes the form $F = F_0 + F_1 Re^2$, where F_0 is the dimensionless Stokes-flow drag force and F_1 is a coefficient that depends on the direction of the flow (Koch & Ladd 1997). Nevertheless, it is a good approximation at the moderate Reynolds numbers of interest here. Although F increases almost linearly with Re, there is a tendency for $\partial F/\partial Re$ to decrease slowly with increasing Re, particularly at the largest Reynolds numbers shown. Simulations with a larger cylinder radius of 41.8 lattice units (filled circles) show that this is not because of the diminishing grid resolution with increasing Reynolds number.

Also shown in figure 21 is the dimensionless streamwise component of the drag force on cylinder number 11, obtained from the simulations of flow in wall-bounded arrays of cylinders with solid volume fractions of 0.204 (squares) and 0.249 (diamonds). The dimensionless drag force was calculated by averaging the streamwise component of the drag force on the cylinder and using the velocity averaged over the entire computational domain. With bounding walls, F increases linearly with Re over the entire range of Reynolds numbers, in contrast to the slight decrease in $\partial F/\partial Re$ with Re for the unbounded periodic domain.

The linear dependence of F on Re may be attributed to the constrained flow direction and, hence, the approximately self-similar velocity field with increasing Reynolds number. Note that, when the direction of the pressure gradient is fixed and the direction of the average velocity is allowed to change, $\partial F/\partial Re$ decreases much more rapidly with increasing Re (Koch & Ladd 1997), because the spatially averaged velocity becomes increasingly aligned with the primary axis of the array.

The drag force on cylinder number 11 – the cylinder furthest from the bounds of the computational domain – is practically the same as the average drag force on all the

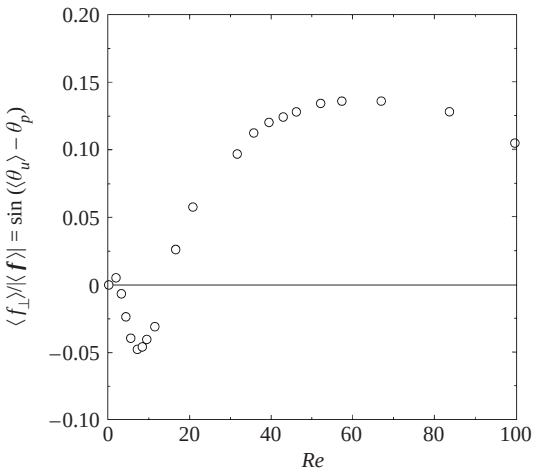

FIGURE 22. The cross-stream component of the average drag force as a function of the Reynolds number from lattice-Boltzmann simulations of flows in an unbounded periodic array of cylinders with $(c, \theta_u, a) = (0.193, \pi/6, 24.8)$, where a is in lattice units. The horizontal line corresponds to Stokes flow ($Re = 0$), for which the cross-stream component of the average drag force is identically zero and the average pressure gradient is in the same direction as the spatially averaged velocity.

cylinders and the walls (see figure 23). Furthermore, for solid volume fractions of 0.214 and 0.249, the dimensionless drag forces, in the range of Reynolds numbers where they increase linearly with the Reynolds number, are given to a good approximation by the fits $F = 47.9 + 4.02Re$ and $F = 65.1 + 4.36Re$, respectively. Assuming a linear dependence of the coefficients on the solid volume fraction, the dimensionless drag force is approximately $F = 37.6 + 3.82Re$ at a solid volume fraction of 0.193. Over the same range of Reynolds numbers, this equation gives almost exactly the same drag force as obtained directly from the simulations of flows in the unbounded periodic domain. The bounding walls, therefore, do not significantly affect the average drag forces on the cylinders furthest from the walls.

10.2. *Lift force*

The cross-stream component of the drag force on the cylinders in an unbounded periodic array, shown in figure 22 as a function of the Reynolds number, may be as large as 10% of the total drag force. Assuming that similar behaviour occurs with the presence of bounding walls, these results show that a considerable pressure gradient may develop across the width of such a channel. This pressure gradient would drive a neutrally buoyant particle in the fluid toward the upper wall of the channel in figure 18. It is interesting to note that there is a relatively small range of Reynolds numbers where the cross-stream component of the drag force is actually negative, i.e. where θ_p is greater than θ_u.

10.3. *Spatial and temporal fluctuations*

The average and standard deviation of the fluctuating drag forces on each of the cylinders in the simulations with bounding walls, at nominal Reynolds numbers of approximately 0, 25, 45 and 80, respectively, are shown in figure 23. Both the streamwise (circles) and cross-stream (squares) components of the drag forces are shown. The abscissa identifies the cylinders whose positions in the channel are shown in figure 1. Note that the upper and lower walls were treated as a single entity in the

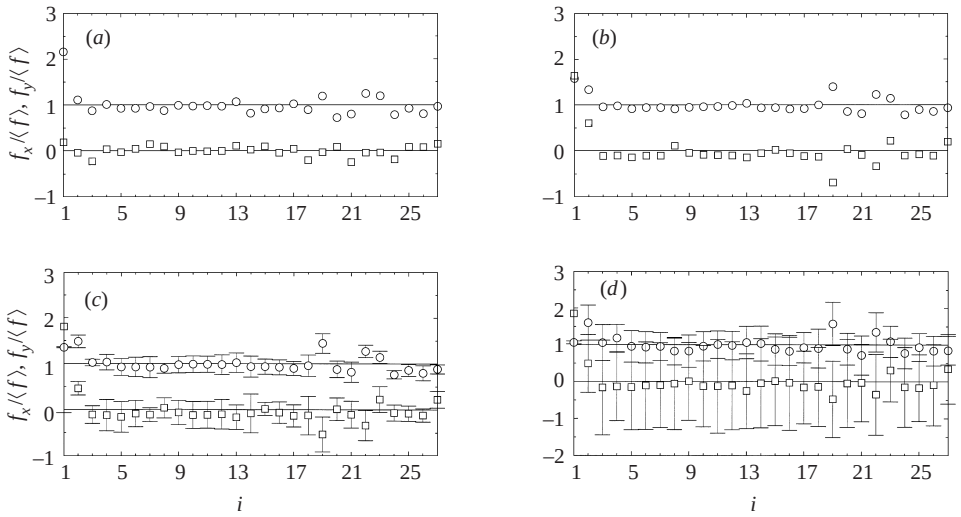

FIGURE 23. The streamwise (circles) and cross-stream (squares) components of the forces, non-dimensionalized with the average drag force, on the 26 cylinders ($i = 2 \ldots 27$) and the wall ($i = 1$). These results are from lattice-Boltzmann simulations of flows in wall-bounded periodic arrays of cylinders with $(c, a) = (0.214, 12.8)$, where a is in lattice units. The positions of the cylinders within the channel are shown in figure 1, and the 'error' bars indicate one standard deviation in the temporal fluctuations. (*a*) $Re = 3.34 \times 10^{-3}$, (*b*) $Re = 25.4$ (steady), (*c*) $Re = 43.6$, (*d*) $Re = 79.5$.

simulations, owing to the use of periodic boundary conditions, and in the following discussion the upper and lower walls will be referred to as a single wall, identified by $i = 1$.

The streamwise component of the drag force on the wall is proportional to its surface area, which is approximately 7.5 times larger than that of a single cylinder. Since the cylinders also have a form-drag contribution, the streamwise component of the drag force on the wall is actually much less than 7.5 times that on a single cylinder.

The cross-stream component of the drag force on the wall is because of the cross-stream pressure gradient generated by the lift forces on the cylinders. Consequently, the cross-stream component of the drag force on the wall is equal to the negative of the sum of the cross-stream components of the forces on all the cylinders. For unsteady flows, the fluctuating force on the wall is very large, and hence the 'error' bars, which indicate one standard deviation of the fluctuations from the mean, cannot be seen on the axes used in figure 23. Note that part of the contribution to this fluctuating force is from the spurious fluctuating cross-stream momentum discussed in § 4.

The cylinders whose drag force appears to be far from the average are those very close the walls – cylinders 2, 19 and 22, for example. The cross-stream components of the drag forces on these cylinders are significantly larger than those on the cylinders closer to the channel centreline. Furthermore, the cross-stream component of the drag force on these cylinders acts toward the channel centreline, whereas the drag force on the cylinders away from the walls is in the negative y-direction, as should be expected based on the lift force shown in figure 22.

It is interesting to note that the lift forces on the cylinders closest to the walls are particularly large because of the effects of fluid inertia. This can be seen by

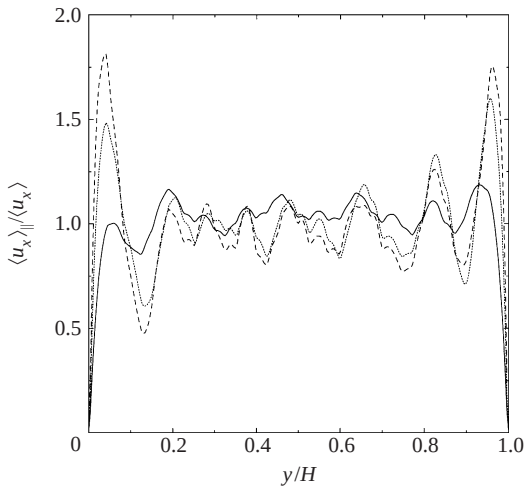

FIGURE 24. The time-averaged streamwise component of the velocity, averaged along the length of the channel, as a function of the distance across the channel width. These results are from lattice-Boltzmann simulations of flows in a wall-bounded array of cylinders with $(c, a, H) = (0.204, 12.8, 246)$, where a and H are in lattice units. The lines correspond to Reynolds numbers of 3.34×10^{-3} (solid), 25.4 (dotted) and 79.5 (dashed).

comparing the cross-stream components of the drag forces on cylinders 2, 19 and 22 in figure 23(*a*) with those in figures 23(*b*) and 23(*c*). Recall that, at finite Reynolds numbers, the fluid velocity between these cylinders and the channel walls was shown in figure 20, for example, to be significantly faster than the average, whereas for Stokes flow, the velocity there is relatively slow.

The length scale over which the walls affect the average velocity at macroscopic or continuum length scales is indicated by the velocity profiles shown in figure 24 for nominal Reynolds numbers of 0, 25 and 80. The time-averaged streamwise component of the velocity is averaged over the length of the channel. Maier *et al.* (1998) showed similar results for a randomly packed cylinder of spheres, but the range of Reynolds numbers was considerably smaller than considered here. Clearly, it is only at finite Reynolds numbers that the fluid is able to maintain a large velocity close to the walls. This effect is similar to that indicated by the simulations of Andrade *et al.* (1997), whereby fluid flowing through a two-dimensional random array of squares undergoes much smaller changes in direction at finite Reynolds numbers than Stokes flow in the same geometry.

10.4. *Spatial correlation*

The dye tracer used in the experiments clearly identified a breaking of spatial periodicity at Reynolds numbers where the velocity fluctuations are chaotic (Hill 2001). Consequently, the temporal velocity fluctuations, and hence the fluctuating drag forces on the cylinders, become uncorrelated at distances beyond their periodic unit cell.

Table 2 shows the correlation coefficients, obtained from simulations, of the x- and y-components of the drag forces on various pairs of cylinders at a Reynolds number of 78.4. The correlation coefficient for cylinders i and j is

$$\rho_{ij} = \langle f_i' f_j' \rangle / (\langle f_i'^2 \rangle \langle f_j'^2 \rangle)^{1/2}, \tag{17}$$

where $f' = f - \langle f \rangle$ is the deviation of either the x- or y-component of the drag force from its respective time-averaged value. Because of the finite size of the computational

r	j	ρ_{ij} (x)	ρ_{ij} (y)
L	5	0.231	0.225
	17	0.123	0.236
	12	−0.117	0.300
	10	−0.0270	0.243
$\sqrt{2}L$	6	−0.132	0.544
	16	−0.0266	0.520
	18	0.126	0.105
	4	0.175	0.323
$\sqrt{5}L$	13	0.135	0.326
	9	0.0827	0.410
	22	−0.0580	0.00932
	24	−0.0157	0.145

TABLE 2. Correlation coefficients of the x- and y-components of the drag force on cylinder number 11 with its nearest (upper section), next-nearest (middle section) and next-next-nearest neighbours (lower section). These results are from lattice-Boltzmann simulations of flow in a wall-bounded array of cylinders with $(c, a, Re) = (0.214, 12.8, 79.5)$. The positions of the cylinders ($i = 11$) and j in the computational domain are shown in figure 1.

domain, correlation coefficients averaged over all pairs of cylinders with the same separation vector $\boldsymbol{r}_{ij}$ are not shown. However, the successive pairs in table 2 do have the same $\boldsymbol{r}_{ij}$, and hence the difference between them gives some indication of the spatial inhomogeneity.

Clearly, the spatial periodicity is broken by the presence of the bounding walls. The strongest correlation in the x- and y-components of the drag forces occurs between nearest and next-nearest neighbouring cylinders, respectively, and the correlation depends very much on the direction of $\boldsymbol{r}$, not just its magnitude.

11. Summary

The lattice-Boltzmann method has been used to compute moderate-Reynolds-number flows in unbounded and wall-bounded periodic arrays of aligned cylinders. Direct, quantitative comparisons of the wake length, for steady flows, and the fundamental frequency, for unsteady flows, were made with experimental measurements. From the simulations, details of the flows, such as the spatial and temporal fluctuations of the fluid velocity and forces on the cylinders, as well as time-averaged values, were examined.

For steady flows, the lengths of wakes behind the cylinders in an unbounded periodic array were in good agreement with those measured experimentally. Therefore, the distance over which the walls influence the flow is comparable to the cylinder separation. For unsteady flows, however, the fundamental frequencies from the simulations of flows in unbounded periodic arrays of cylinders were significantly higher than those for wall-bounded arrays. Under these conditions, the walls affect the flows everywhere in the domain, not just close to the walls.

With the onset of unsteady flow in the wall-bounded arrays of cylinders, the spatial periodicity, at the length scale of the cylinder separation, is broken. This increases

the effective length of the wakes behind the cylinders, and results in slower dynamics, because it takes longer for disturbances to convect the larger distance.

For unbounded periodic arrays of cylinders, the transition to unsteady flow occurs via a super-critical Hopf bifurcation, and the transition to chaotic dynamics occurs via a sequence of period-doubling bifurcations. With bounding walls, however, the transition to chaotic dynamics occurs via quasi-periodicity, and the transition occurs at much smaller Reynolds numbers.

This work was funded by the National Science Foundation (NSF) and the National Aeronautics and Space Administration (NASA) under grant numbers CTS-9526149 and NAG3-2440, respectively. The computations were performed using the resources of the Cornell Theory Center. We would also like to thank Suwimon Apariki for her assistance in performing the experiments and Anthony J. C. Ladd for providing the original lattice-Boltzmann code.

REFERENCES

Aidun, C. K., Lu, Y. & Ding, E.-J. 1998 Direct analysis of particulate suspensions with inertia using the discrete Boltzmann equation. *J. Fluid Mech.* **373**, 287–311.

Andrade, J. S., Almeida, M. P., Mendes Filho, J., Havlin, S., Suki, B. & Stanley, H. E. 1997 Fluid flow through porous media: The role of stagnant zones. *Phys. Rev. Lett.* **79**, 3901–3904.

Bittleston, S. H. 1986 Flows past arrays of cylinders. PhD thesis, University of Bristol.

Ghaddar, C. K. 1995 On the permeability of unidirectional fibrous media: A parallel computational approach. *Phys. Fluids* **7**, 2563–2586.

Hasimoto, H. 1959 On the periodic fundamental solution of the Stokes equations and their application to viscous flow past a cubic array of spheres. *J. Fluid Mech.* **5**, 317–328.

Hill, R. J. 2001 The effects of fluid inertia on flows in porous media. PhD thesis, Cornell University.

Hill, R. J., Koch, D. L. & Ladd, A. J. C. 2001*a* The first effects of fluid inertia on flows in ordered and random arrays of spheres. *J. Fluid Mech.* **448**, 213–241.

Hill, R. J., Koch, D. L. & Ladd, A. J. C. 2001*b* Moderate-Reynolds-number flows in ordered and random arrays of spheres. *J. Fluid Mech.* **448**, 243–278.

Koch, D. L. & Brady, J. F. 1985 Dispersion in fixed beds. *J. Fluid Mech.* **154**, 399–427.

Koch, D. L. & Ladd, A. J. C. 1997 Moderate Reynolds number flows through periodic and random arrays of aligned cylinders. *J. Fluid Mech.* **349**, 31–66.

Ladd, A. J. C. 1994*a* Numerical simulations of particulate suspension via a discretized Boltzmann equation. Part 1. Theoretical foundation. *J. Fluid Mech.* **271**, 285–309.

Ladd, A. J. C. 1994*b* Numerical simulations of particulate suspension via a discretized Boltzmann equation. Part 2. Numerical results. *J. Fluid Mech.* **271**, 311–339.

Maier, R. S., Kroll, D. M., Kutovsky, Y. E., Davis, H. T. & Bernard, R. S. 1998 Simulation of flow through bead packs using the lattice-Boltzmann method. *Phys. Fluids* **10**, 60–74.

Qi, D. 1999 Lattice-Boltzmann simulations of particles in non-zero-Reynolds-number flows. *J. Fluid Mech.* **385**, 41–62.

Sangani, A. S. & Acrivos, A. 1982 Slow flow through a periodic array of spheres. *Intl J. Multiphase Flow* **8**, 343–360.

Schatz, M. F., Dwight, B. & Swinney, H. L. 1995 Instability in a spatially periodic open flow. *Phys. Fluids* **7**, 344–358.

Taneda, S. 1956 Experimental investigation of the wake behind a sphere at low Reynolds numbers. *J. Phys. Soc. Japan* **11**, 1104–1108.

Wiggins, S. 1990 *Introduction to Applied Nonlinear Dynamical Systems and Chaos*, chap. 3. Springer.

Williamson, C. H. K. 1989 Oblique and parallel modes of vortex shedding in the wake of a circular cylinder at low Reynolds numbers. *J. Fluid Mech.* **206**, 579–627.